High-Resolution Upwind Scheme for Vortical-Flow Simulations

Kozo Fujii*
Institute of Space and Astronautical Science, Kanagawa, 229 Japan
and
Shigeru Obayashi†
NASA Ames Research Center, Moffett Field, California 94035

One of the high-resolution upwind schemes called "MUSCL with Roe's average" is applied to vortical flow simulations. Two examples are considered. One is the leading-edge, separation-vortex flow over a strake-delta wing. The other is a high angle-of-attack supersonic flow over a space-plane-like configuration. The comparison with the central-difference solutions indicates that the present upwind scheme is less dissipative and thus has better resolution for the vortical flows. Thus, it is concluded that the use of proper unwind schemes is recommended for vortical flow simulations at a high Reynolds number, and verification of computed result is especially important for vortical-flow simulations.

Introduction

THE flow over aircraft and missiles at moderate to high angles of attack is characterized by the presence of large spiral vortices on the leeward side of the body. These separation vortices induce low pressure on the body upper surface, and this low pressure is the predominant factor of the resulting aerodynamic characteristic of the body. Research on such flow is of great importance practically as well as physically because understanding of the separated and vortical flowfields may lead to the control of vortex behavior and eventually to the enhancement of flight vehicle performance.

The rapid progress of supercomputers and numerical methods has made computer simulation of such vortical flows feasible. Recent efforts in computational methods and application results were surveyed by Newsome and Kandil.[1] Three-dimensional, Reynolds-averaged, Navier-Stokes equations used for various flow simulations have become a primary method for the vortical-flow simulations since they can describe separated vortical flows with no special treatment. There exists one important fact that should be kept in mind. Typical computational grids used for high-Reynolds-number, Navier-Stokes simulations are fine only near the body surface to resolve viscous layers. These grid distributions are adequate for those flows where important phenomena only occur near the body surface as embedded shock waves or flow separation. For vortical-flow simulations, on the other hand, not only the region near the body surface but also regions away from the body surface are important. Since the strength of vortices which are located away from the body is a dominant factor of the flowfield, grid resolution away from the body is critical for an accurate simulation of vortical flow. Rai in Ref. 2 pointed out that conventional, spatially second-order-accurate, finite-difference schemes are much too dissipative for calculations involving vortices that travel large distances. Reference 3 includes a study of the effect of grid resolution for vortical-flow simulations and found the important result that the vortex breakdown phenomenon cannot be predicted unless a sufficiently fine grid is used.

Now, how can we obtain accurate solutions for the vortical flows with computer memory and time constraints? High-order, upwind differencing has become popular in recent Euler methods for compressible inviscid flows. This feature has been extended in the straightforward manner for the evaluation of the convective terms of Navier-Stokes computations (see Refs. 4–6, for instance.) Discontinuities are more sharply captured by these upwind methods than those captured by the conventional central-difference method with additional numerical dissipation since high-order upwind methods introduce minimum amount of dissipation needed to prevent oscillations. Recently, the matrix form of the dissipation terms implicitly introduced by upwind methods was studied[7–9] and it was shown that such terms in the upwind schemes such as Roe's flux difference splitting become small in the viscous layers. As artificial dissipation should be kept to a minimum and viscous effects near the body surface should be correctly evaluated in vortical-flow simulations, the high-resolution upwind method may be adequate for vortical-flow simulations.

The objective of the present work is to demonstrate the capability of the high-resolution upwind method for accurate vortical-flow simulations. Two flowfields are considered as application examples. One is a subsonic flow over a strake-delta wing. Simulation of the same flowfield was already conducted by the first author using a conventional central-difference method.[3] The same grid distributions, fine grid and medium grid, are used for comparison. The second example is a supersonic flow over a space-plane configuration proposed for the research at the National Aerospace Laboratory. The flowfield is much more complicated in this example since there exists bow shock wave, wing shock wave, fuselage vortex, and wing vortex.

Governing Equations and Numerical Algorithm

Compressible Navier-Stokes Equations

The basic equations under consideration are the unsteady Navier-Stokes equations written for a body-fitted coordinate system (ξ,η,ζ) with the thin-layer approximation

$$\partial_\tau \hat{Q} + \partial_\xi \hat{E} + \partial_\eta \hat{F} + \partial_\zeta \hat{G} = Re^{-1}\partial_\zeta \hat{S} \tag{1}$$

The use of thin-layer, Navier-Stokes equations is justified because the viscous effects are confined to a thin layer near the

Presented as Paper 89-1955 at the AIAA 9th Computational Fluid Dynamics Conference, Buffalo, NY, June 13-15, 1989; received April 8, 1989; revision received Aug. 2, 1989.

*Associate Professor. Member AIAA.
†National Research Council (NRC) Research Associate. Member AIAA.

wall and are dominated by the viscous terms associated with the strain rates normal to the wall and because the flow away from the body is essentially rotational inviscid. The contribution of the viscous terms in the shear layer rolling up from the surface wall and core of the vortices is assumed to be negligible. It should be noted that the viscous terms are not properly evaluated in these regions even by the full Navier-Stokes equations because of the grid deficiency.

The pressure, density, and velocity components are related to the energy for an ideal gas by

$$p = (\gamma - 1)\left[e - \frac{1}{2}\rho\,(u^2 + v^2 + w^2)\right] \tag{2}$$

LU-ADI Algorithm with Upwind Feature

The time-integration algorithm used here is the LU-ADI factorization method proposed by Obayashi et al.[10] for two-dimensional problems. An extension to three-dimensional problems is described in Ref. 11. This algorithm decomposes the usual block tridiagonal system of Beam and Warming's into the product of lower- and upper-scalar bidiagonal matrices using a diagonal form and an approximate LDU decomposition. The basic algorithm is first-order accurate in time. In this original LU-ADI scheme, the convective terms are evaluated using second- or fourth-order central differencing, and the viscous terms are evaluated using second-order central differencing in the right-hand side. Since the delta form is used, steady-state solutions are indifferent to the left-hand-side operators and depend only on the right-hand-side steady-state description. Thus, even though the rate of convergence and the stability may be influenced by the choice of left-hand side, steady-state solutions can be improved simply by modifying the right-hand-side discretization method.

In the right-hand side, convective terms are now evaluated using flux-difference splitting by Roe.[12] The Monotonic Upstream Schemes for Conservation Laws (MUSCL) interpolation is used for the higher-order extension, and the detail is found in Ref. 9 but is briefly described again here. When the convective terms are differenced with the flux-difference splitting of Roe, the spatial derivatives are written in the conservative form as a flux balance. For instance in the ξ direction,

$$\left(\frac{\partial \hat{E}}{\partial \xi}\right)_j = \frac{(\tilde{E}_{j+\frac{1}{2}} - \tilde{E}_{j-\frac{1}{2}})}{\Delta\xi} \tag{3}$$

The numerical flux $\tilde{E}_{j\pm\frac{1}{2}}$ can be written as the solution to an approximate Riemann problem, and the necessary metric terms are evaluated at the cell interfaces $j + \frac{1}{2}$

$$\tilde{E}_{j+\frac{1}{2}} = \tfrac{1}{2}[\bar{E}(Q_L) + \bar{E}(Q_R) - |\bar{A}|(Q_R - Q_L)]_{j+\frac{1}{2}} \tag{4}$$

where $\bar{E}$ is the flux vector and $\bar{A}$ is the corresponding Jacobian matrix computed using the Roe's average state. The Q_L and Q_R are the state variables to the left and right of the half-cell interface. These state variables are determined from the locally one-dimensional nonoscillatory interpolations called MUSCL approach. Primitive variables $q\,[\rho,u,v,w,p]^T$ are used for that purpose, and high-order accurate monotone differencing is given by a one-parameter κ

$$(q_L)_{j+\frac{1}{2}} = q_j + (s/4)[(1 - \kappa s)\Delta_- + (1 + \kappa s)\Delta_+]_j$$

$$(q_R)_{j+\frac{1}{2}} = q_{j+1} - (s/4)[(1 - \kappa s)\Delta_+ + (1 + \kappa s)\Delta_-]_{j+1} \tag{5}$$

where

$$(\Delta_+)_j = q_{j+1} - q_j, \qquad (\Delta_-)_j = q_j - q_{j-1}$$

$$s = \frac{2\Delta_+\Delta_- + \epsilon}{(\Delta_+)^2 + (\Delta_-)^2 + \epsilon}$$

where s is the Van Albada's limiter and ϵ is a small constant to prevent zero division. For all of the results here, third-order accuracy corresponding to $\kappa = \frac{1}{3}$ is used. Near the boundary, the MUSCL interpolation goes back to the first order.

Central differencing that is adopted in the original LU-ADI code is used just for the comparison. In that case, nonlinear artificial dissipation terms are added (see Ref. 13). When considering the dissipation term as a part of the flux evaluation, the numerical flux $\tilde{E}_{j+\frac{1}{2}}$ in the ξ direction can be written as

$$\tilde{E}_{j+\frac{1}{2}} = \tfrac{1}{2}\{\hat{E}_j + \hat{E}_{j+1} - (\sigma J^{-1})_{j+\frac{1}{2}}$$

$$[(1 - \varphi)\epsilon_2 - \varphi\epsilon_4 \nabla_\xi \Delta_\xi]_{j+\frac{1}{2}}\}(Q_{j+1} - Q_j) \tag{6}$$

where σ is a spectral radius and φ is a limiter-like function that is determined by the local flow gradient. Their coefficients ϵ_2 and ϵ_4 are set to be 0.04, which were reasonable values that have been successfully used for many practical computations.

Results

Computed Results for Subsonic Flow over a Strake-Delta Wing

The first example is the subsonic flow over a strake-delta wing. The flowfield was extensively studied experimentally by Brennenstuhl and Hummel[14] in a low-speed wind tunnel and computationally by one of the present authors.[15] The free-stream Mach number is 0.3, and the Reynolds number based on the root chord is 1.3×10^6 in the following computations.

The angle of attack for the first case is 12 deg. At this angle of attack there exist two vortices over the upper surface of the wing: one emanating from the strake leading edge and the other from the main-wing leading edge. These two vortices merge together over the main-wing surface because of the mutual interaction. Figures 1a and 1b show the overall view of the spanwise total pressure contour plots at several chordwise stations. The contours are plotted at 35–95% chordwise stations with 10% increase. The result shown in Fig. 1a is obtained by the upwind differencing and the result shown in Fig. 1b by the central differencing (with added artificial dissipa-

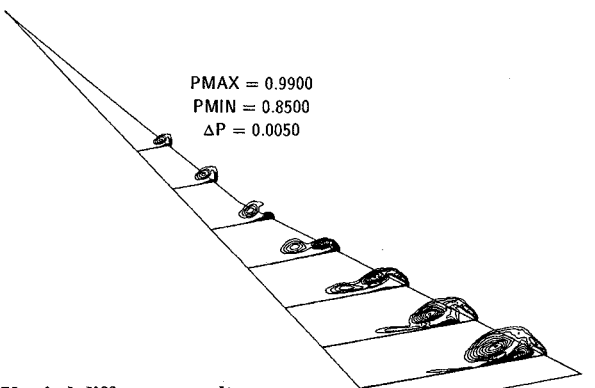

a) Upwind difference result

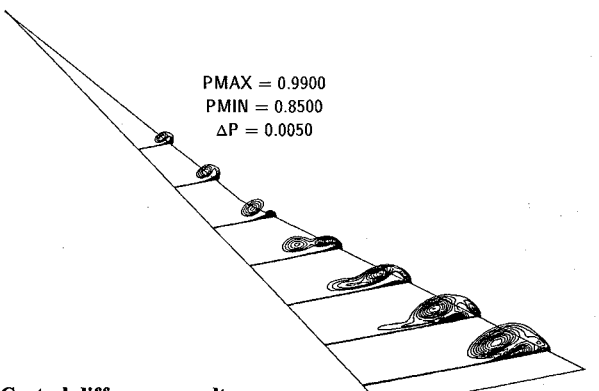

b) Central-difference result

Fig. 1 Spanwise total pressure contour plots: $\alpha = 12$ deg—overall view of the fine grid solution.

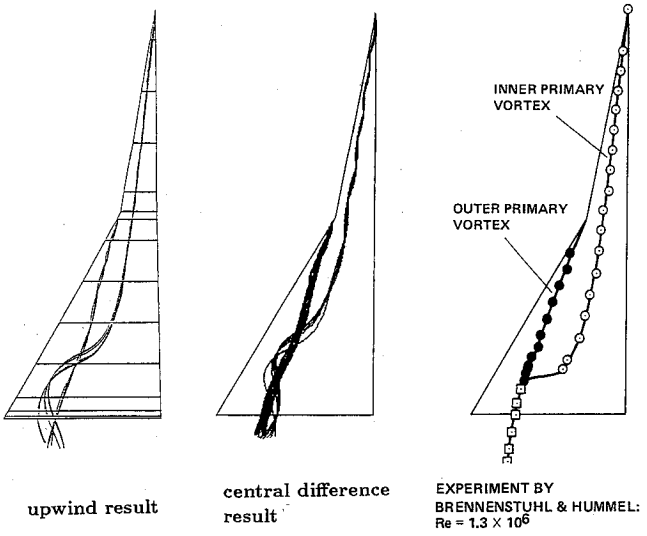

Fig. 2 Computed vortex trajectories for the upwind result: $\alpha = 12$ deg.

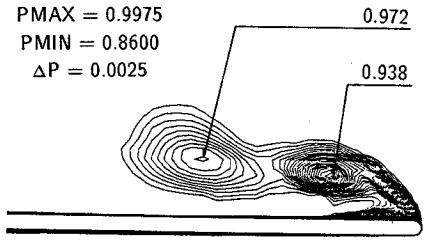

a) Total pressure contour

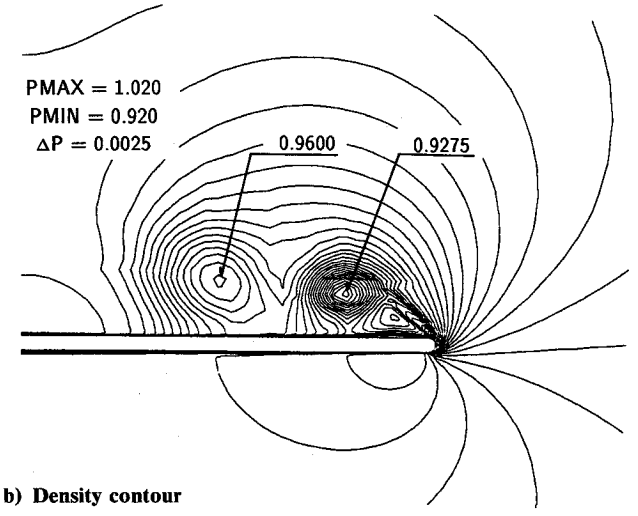

b) Density contour

Fig. 3 Spanwise contour plots at 65% chord by the upwind scheme: $\alpha = 12$ deg.

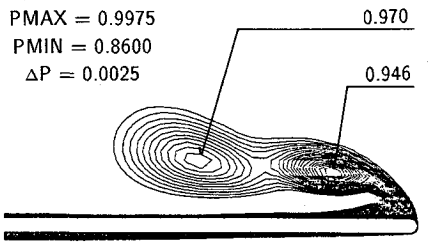

a) Total pressure contour

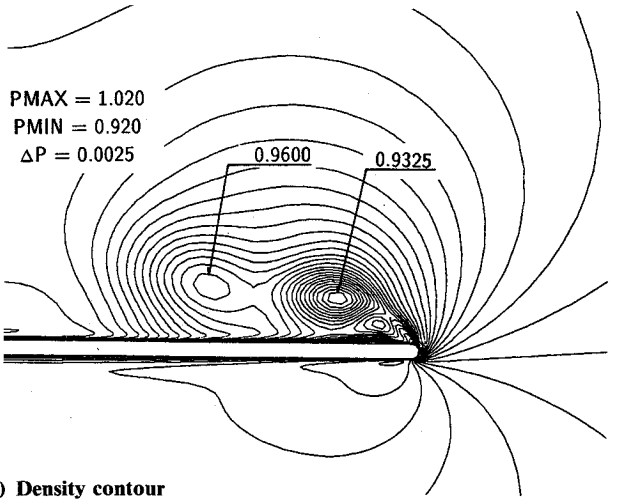

b) Density contour

Fig. 4 Spanwise contour plots at 65% chord by the central-difference scheme: $\alpha = 12$ deg.

tion). The total number of grid points is about 850,000: 119 points in the chordwise direction, 101 points circumferentially, and 71 points in the normal direction. Details of the grid generation and the grid distribution can be found in Ref. 15. Both results indicate the existence of two vortices over the wing surface and their interaction. It seems that the merging of the two vortices moves downstream in the upwind solution.

The corresponding particle path traces showing the vortex trajectories are shown in Fig. 2 for the upwind result. The comparison of the computed vortex trajectories with the experiment that was already done for the central differencing result in Ref. 15 is also presented in this figure. It is clear that merging of two vortices moves downstream in the upwind result, compared to the central result, but still occurs upstream than the experiment at the same Reynolds number.

For further comparison, the spanwise total pressure contour plots (with twice the number of contours lines) and density contour plots at 65% chordwise location are depicted in Figs. 3 and 4. Figures 3a and 3b are the results obtained by the upwind differencing, and Figs. 4a and 4b are the results by the central differencing. Both contour plots show strong gradients due to the viscous layers near the surface. The upwind result shows that this region is thinner compared to the central-differencing result. This may be reasonable since numerical dissipation introduced by the present upwinding is small in the viscous boundary layers as explained in Ref. 9.

The same computation was carried out using a smaller number of grid points (called medium grid in Ref. 3, about 120,000 in total). Compared to the previous grid, the number of the grid points is decreased in all of the directions. Figures 5a and 5b represent the total pressure contour plots obtained by the upwind and central-difference computations, respectively. The contours are again plotted at 35–95% chordwise stations with a 10% increase. The upwind result shown in Fig. 5a indicates the existence of two vortices and their merging process; although the inner vortex is not as distinct as the fine-grid solution. On the other hand, the central-difference result in Fig. 5b shows only one flattened vortex instead of two vortices.

The angle of attack for the second case is 30 deg. The previous study in Ref. 15 showed that vortex breakdown takes place near the trailing edge both in the experiment and in the computational results on the fine grid. Here medium-grid (previously mentioned grid of about 120,000 points) computations are carried out with the central differencing and the upwind differencing. The computed total pressure contour plots are presented in Figs. 6a and 6b. An abrupt increase of the vortex core is observed near the trailing edge in the upwind result shown in Fig. 6a. This indicates that the vortex has undergone breakdown. In fact, the plot of the streamwise velocity (although not shown here) showed that there exists the

reverse flow region near the trailing edge. The central-difference result shown in Fig. 6b, on the other hand, does not show such a sudden change. Again, the resolution is enhanced by the use of the present upwind scheme at least on the grid used here (although a slight increase of the number of grid points may introduce the breakdown phenomenon also in the central-difference result).

It is recognized from these results that the present upwind scheme has better resolution than the conventional central-difference scheme on the same grid; although grid resolution itself is, of course, an important factor for an accurate flow simulation. The upwind scheme is more "vortex-preserving" than the central-differencing scheme (with added dissipation) since it has a lower level of dissipation (see also Ref. 2).

In the artificial dissipation model used with the central difference, the magnitude of the coefficient is the same for all of the equations. Suppose we decompose the Euler equations into a set of independent equations for the waves with the characteristic speed u, $u + c$, $u - c$ the magnitude of coefficient should be chosen to be sufficiently large for any of the waves to maintain stability. In the flux evaluation of the Roe's flux-difference splitting, this coefficient is in the form of matrix A. If you rewrite this dissipation term, it is recognized that dissipation works on α, the strength of each wave,[8] and the magnitude is automatically determined for each wave by the upwinding process. Thus, artificial dissipation terms included in the high-resolution upwind methods could be smaller than the dissipation used with the central-difference methods. That explains why the upwind method shows better resolution in the computed results shown in this paper.

Note that there is an effort to improve artificial dissipation models used with the central differencing (see for instance, Ref. 16). Such models, however, need matrix conditioning and thus require more computer time than conventional artificial dissipation models. It should also be noted that Vatsa et al.[9] demonstrated that the dissipation-like terms in the Roe's upwinding become automatically small in the viscous layers near the body surface in the multidimensional problems.

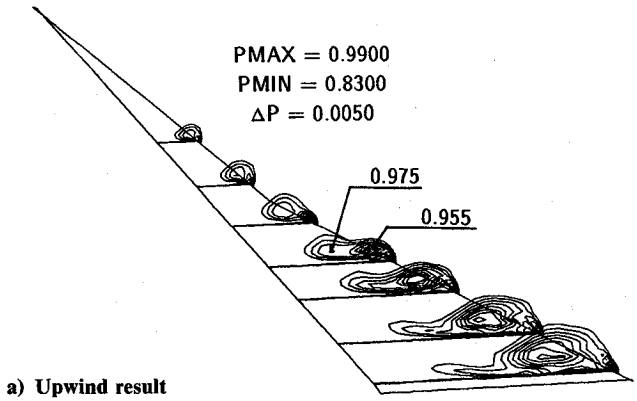

a) Upwind result

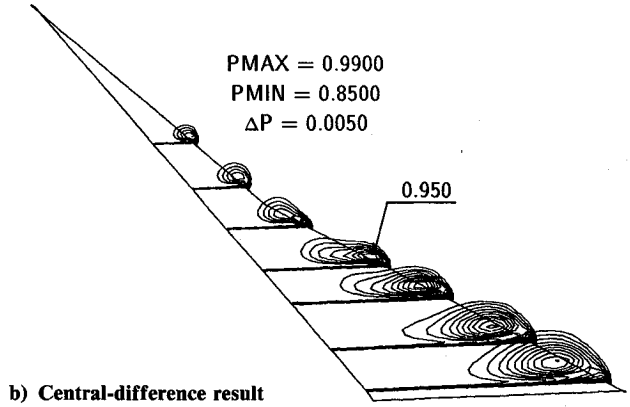

b) Central-difference result

Fig. 5 Computed total pressure contour plots: $\alpha = 12$ deg—overall view of the medium grid solution.

Of course, solutions of both central and upwind difference schemes should converge to the solution of the original partial differential equations as the computational grid is refined. The accuracy estimation based on the idea of the Taylor expansion is important but insufficient for the system of nonlinear equations. What we need in numerical schemes is the better representation of the properties of original partial differential equations and, in that sense, the upwind-difference scheme shows a better result than that of the central-difference scheme for the grid distributions feasible under the memory restriction of the current supercomputers.

Computed Results for Supersonic Flow over a Space Plane

Computations were carried out at a Mach number of 1.5, Reynolds number of 1×10^6 based on the maximum span length, and angle of attack of 20 deg. The configuration has only fuselage and strake wing as is shown in Fig. 7, which is an overview of the surface grid over this geometry. Topologically, the grid is of C-type in the chordwise direction and O-type in the circumferential direction and consists of 89 points in the chordwise direction, 103 points in the circumferential direction, and 40 points from the body to the outer boundary. The minimum spacing near the body surface is almost 1×10^{-4} with the span-length unity. The outer boundary is located outside of the bow shock, which is captured. In the computation, bilateral symmetry is assumed and the half of the volume is solved. At the end of the body geometry, zeroth-order extrapolation is applied as the outflow condition. The modified "Baldwin-Lomax" turbulence model[17] is used in all of the following computations for space-plane configurations. Even for this simplified geometry, the flowfield is complicated since there exists bow shock, strake and wing

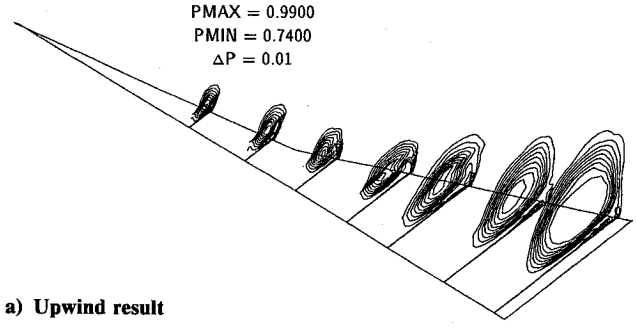

a) Upwind result

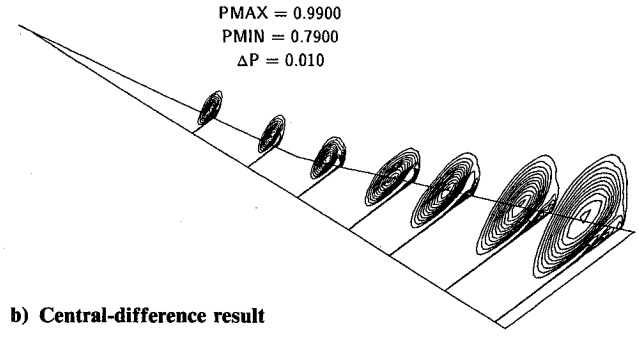

b) Central-difference result

Fig. 6 Computed total pressure contour plots: $\alpha = 30$ deg—overall view of the medium grid solution.

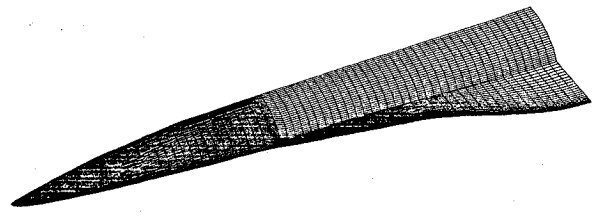

Fig. 7 Overall view of the computational grid for the space plane.

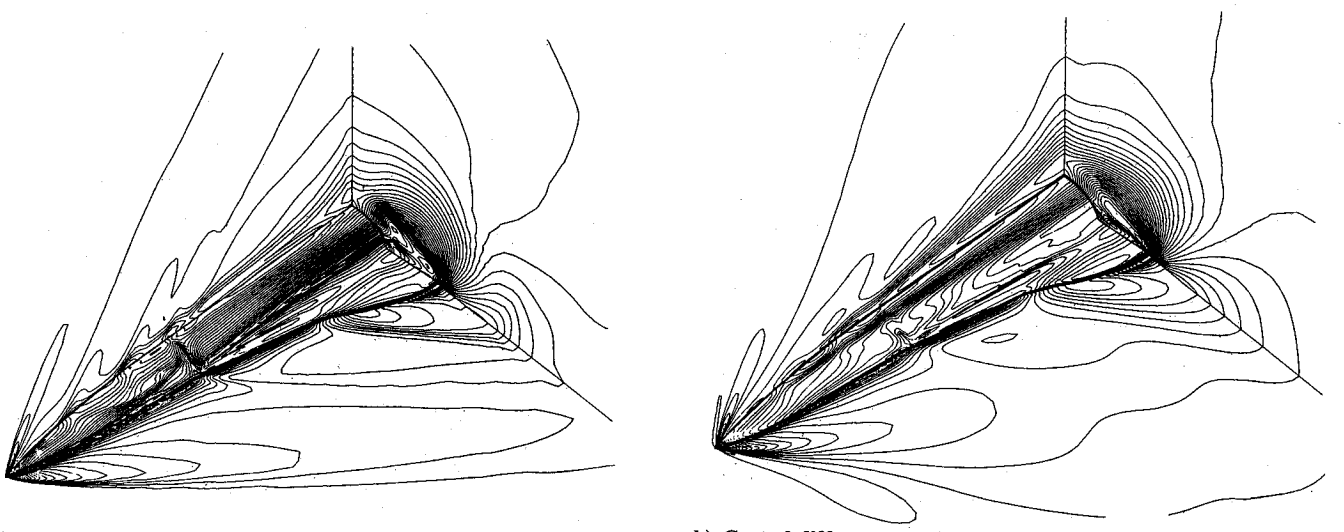

a) Upwind result b) Central-difference result

Fig. 8 Overall view of the computed density contour plots over a space plane: $M_\infty = 1.5$, $\alpha = 20$ deg.

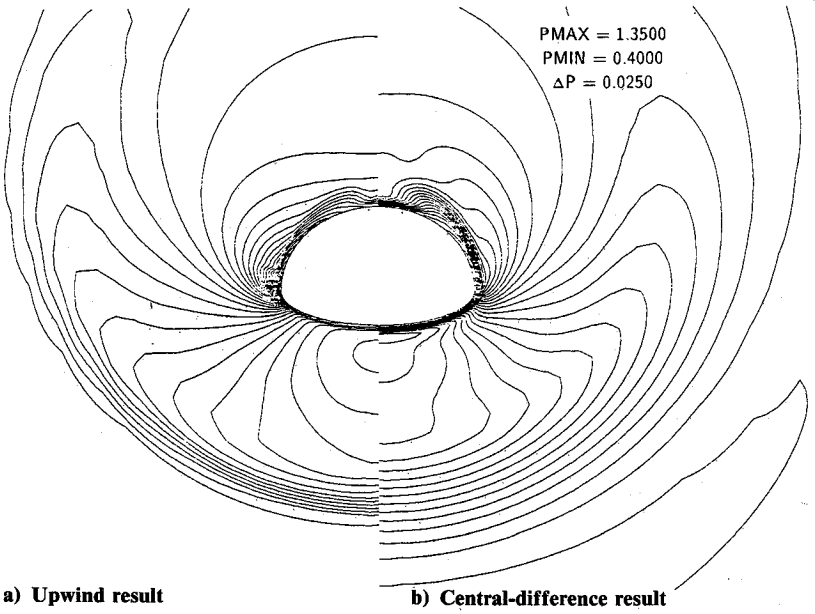

a) Upwind result b) Central-difference result

Fig. 9 Spanwise plots of the computed density contours over a space plane ($x/c = 16\%$): $M_\infty = 1.5$, $\alpha = 20$ deg.

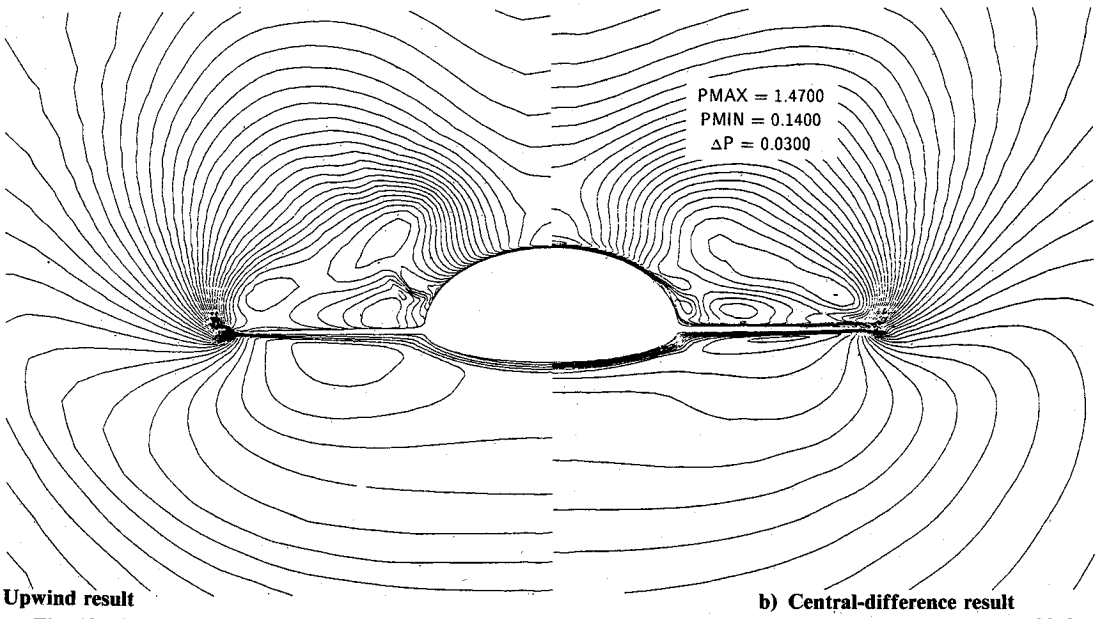

a) Upwind result b) Central-difference result

Fig. 10 Spanwise plots of the computed density contours over a space plane ($x/c = 98\%$): $M_\infty = 1.5$, $\alpha = 20$ deg.

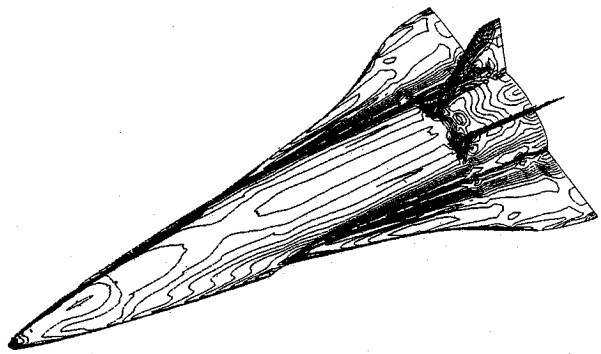

a) Upwind result

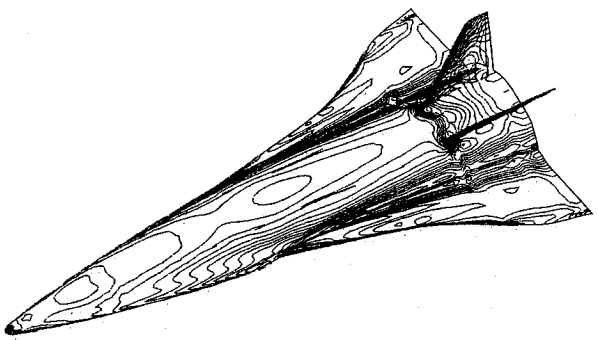

b) Central-difference result

Fig. 11 Overall view of the computed surface-density contour plots over a plane with tail fin: $M_\infty = 1.5$, $\alpha = 15$ deg.

shocks, and leading-edge separation vortices. Thus, it is important to use an accurate solution scheme for linear waves and nonlinear waves. Figures 8a and 8b show the overall density contour plots for the upwind and central-difference solutions, respectively. Since the present upwind scheme is the total variation diminishing type, all of the shock waves, the bow shock wave from the nose, and wing shocks from the strake and the wing are captured better in Fig. 8a than the central-difference result shown in Fig. 8b. It is noticed that contours over the surface especially near the wing-fuselage junction are significantly different between Figs. 8a and 8b. Also noticed is the kink of the contour lines on the fuselage surface where the strake begins. This may be due to the distribution of the grid, and the effect is pronounced when the upwind differencing is used.

Crossflow density plots at the forward fuselage section (= 16% chord) are shown in Fig. 9 with the upwind result presented on the left and the central-difference result on the right. Again, bow shock is better in the upwind result. The central-difference solution demonstrates stronger primary vortex; although both solutions produce the primary vortex. This may be caused by the artificial dissipation terms implemented in the central-difference computation. In other words, the central-difference solution represents sort of relatively "lower Reynolds number flow" near the body surface because of the added dissipation, and thus the flow tends to separate more easily. Note that the minimum spacing in these computations is not sufficiently small, and reducing the minimum spacing would improve the solution for the central differencing. The cross-sectional geometry is composed of the flat segment in the bottom and circular segment on the top. At the junction, another separation may be recognized in the upwind solution although not clearly seen. Figure 10 shows the similar plots for the rear portion of the geometry (= 98% chord). One interesting feature here is the existence of the crossflow shock wave in the upwind solution. Experimental flow visualization for the crossflow was not carried out, and thus it is impossible to say which solution is physically correct. However, it is important that different flowfields are obtained by the two different solution schemes.

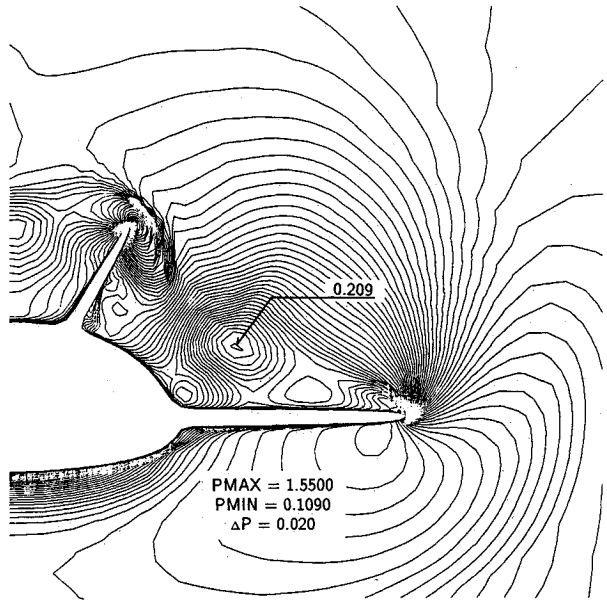

a) Upwind result

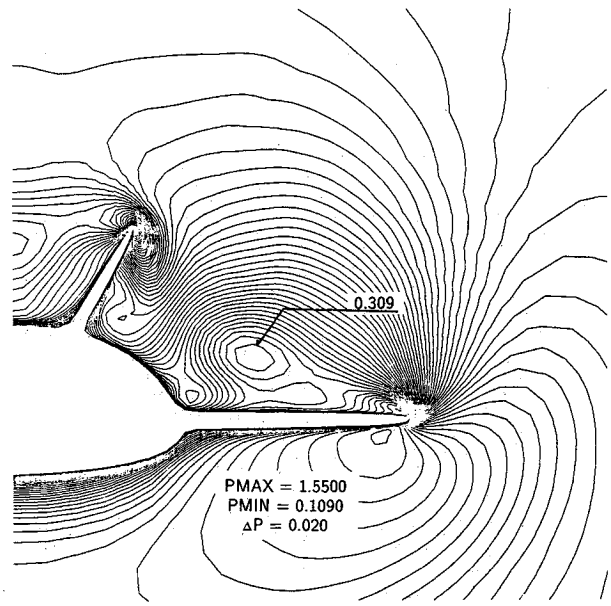

b) Central-difference result

Fig. 12 Spanwise plots of the computed density contours over a space plane with tail fin ($x/c = 91\%$): $M_\infty = 1.5$, $\alpha = 15$ deg.

To compare the result with the experiment, computations for the configuration with the tail fin were also carried out. A similar grid with the total number of about 550,000 points was created. The flow condition was given as the Mach number, 1.5, the Reynolds number, 4×10^6 based on the maximum span length, and the angle of attack, 15 deg. Here again, bilateral symmetry was assumed, and the half of the volume was solved. The minimum spacing near the body surface is now set to be in the range of $2\text{–}5 \times 10^{-5}$ with the span-length unity. Figures 11a and 11b show the surface-density contour plots for the upwind and central-difference solutions, respectively. Both results show similar flow character, although a difference is observed in the number of the contour levels.

Cross-sectional density contour plots at the chordwise station 91% are shown in Figs. 12a and 12b. Fin shock wave is observed in both results, but is better defined in Fig. 12a. No

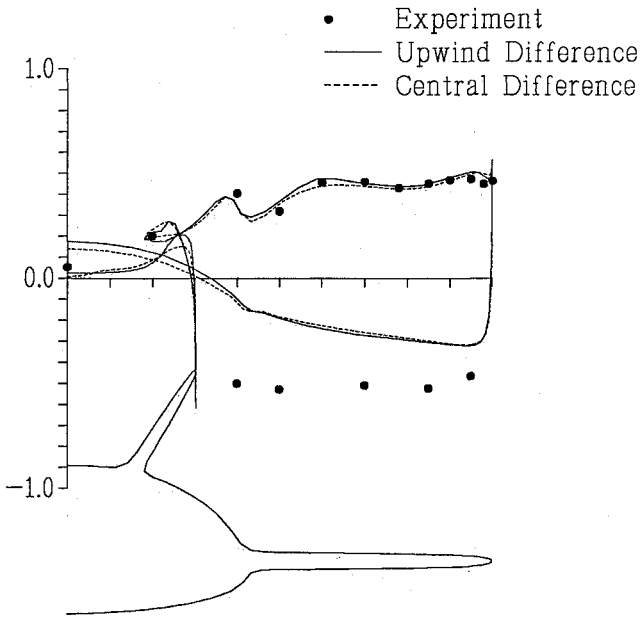

Fig. 13 Spanwise surface C_p plots ($x/c = 91\%$): $M_\infty = 1.5$, $\alpha = 15$ deg.

distinct difference is observed between the two figures except that the minimum contour level corresponding to the core of the separation vortex is significantly different. This wing-fuselage-tail model has a rising slope in the rear portion of the lower body, and the flow expansion is observed there. The flow at this chordwise station is complicated due to the existence of the fin shock wave and leading-edge separation vortices. More discussion about the effect of the tail fin is given in Ref. 17.

Figure 13 shows the computed cross-sectional surface C_p at the same chordwise station. Also plotted is the experimental data obtained at the National Aerospace Laboratory. Note that the disagreement between the experiment and the computations for the lower surface comes from the effect of the model support in the experiment. Either of the computed results shows good agreement with the experiment, although the C_p peak due to vortical flow over the main wing is slightly higher for the upwind result.

Conclusions

One of the high-resolution upwind schemes called MUSCL with Roe's average was applied to vortical-flow simulations. Numerical experiments shown in the present paper indicate that the present upwind scheme has better resolution on the same grid than the central-difference scheme. Thus, it was concluded that the use of proper upwind schemes is recommended for vortical-flow simulations at a high Reynolds number, and verification of computed result is especially important for vortical-flow simulations.

From the solution presented here, another important conclusion may be that it is dangerous to discuss physics of separated vortical flows based on the numerical solutions without sufficient resolution. Verification of the computed results is especially important for vortical-flow simulations, and it may be necessary to simulate the flow field with a sequence of grid cell size even with the high-order upwind schemes.

Acknowledgment

This work was initiated when the first author was a National Research Council Research Associate at NASA Ames Research Center. The authors are deeply indebted to the members of the Applied Computational Fluids Branch and H. Yee at NASA Ames Research Center. The space-plane computation was carried out under the agreement on the cooperative research between the Institute of Space and Astronautical Science and the National Aerospace Laboratory. The authors would like to thank Susumu Takanashi at the National Aerospace Laboratory, Japan, for allowing them to use the grid for the space plane. The computations for the space plane were carried out with the help from Kisa Matsushima, Fujitsu Limited.

References

[1]Newsome, R. W. and Kandil, O. A., "Vortical Flow Aerodynamics—Physical Aspects and Numerical Simulation," AIAA Paper 87-0205, Jan. 1987.

[2]Rai, M. M., "Navier-Stokes Simulations of Blade-Vortex Interaction Using High-Order Accurate Upwind Schemes," AIAA Paper 87-0543, 1987.

[3]Fujii, K., Gavali, S., and Holst, T. L., "Evaluation of Navier-Stokes and Euler Solutions for Leading-Edge Separation Vortices," *International Journal of Numerical Methods in Fluids,* Vol. 8, Oct. 1988, pp. 1319–1329; also NASA TM 89458, June, 1987.

[4]Thomas, J. L., Taylor, S. L., and Anderson K. A., "Navier-Stokes Computations of Vortical Flows over Low Aspect Ratio Wing," AIAA Paper 87-0207, 1987.

[5]Ogawa, S., Ishiguro, T., and Takakura, Y., "Numerical Simulations of Flow Field around Three-Dimensional Complex Configurations," *Proceedings of the 7th GAMM Workshop on Numerical Methods in Fluid Mechanics,* Vieweg, FRG, Sept. 1987.

[6]Klopfer, G. H. and Yee, H. C., "Viscous Hypersonic Shock-On-Shock Interaction on Blunt Cowl Lips," AIAA Paper 87-0233, Jan. 1987.

[7]Van Leer, B., Thomas, J. L., Roe, P. L., and Newsome, R. W., "A Comparison of Numerical Flux Formulas for the Euler and Navier-Stokes Equations," AIAA Paper 87-1104CP, June 1987.

[8]Roe, P. L., "Finite-Volume Methods for the Compressible Navier-Stokes Equations," *Proceedings of the International Conference on Numerical Methods for Laminar and Turbulent Flows,* Pineridge, UK, July 1987.

[9]Vatsa, V. N., Thomas, J. L., and Wedan, B. W., "Navier-Stokes Computations of Prolate Spheroids at Angle of Attack," AIAA Paper 87-2627, 1987.

[10]Obayashi, S., Matsushima, K., Fujii, K., and Kuwahara, K., "Improvements in Efficiency and Reliability for Navier-Stokes Computations Using the LU-ADI Factorization Algorithm," AIAA Paper 86-338, Jan. 1986.

[11]Fujii, K. and Obayashi, S., "Navier-Stokes Simulations of Transonic Flows over a Practical Wing Configuration," *AIAA Journal,* Vol. 25, March 1987, pp. 369–370.

[12]Roe, P. L., "Characteristic-Based Schemes for the Euler Equations," *Annual Review of Fluid Mechanics,* 1986, pp. 337–365.

[13]Fujii, K. and Obayashi, S., "Navier-Stokes Simulations of Transonic Flows over Wing-Fuselage Combination," *AIAA Journal,* Vol. 25, Dec. 1987, pp. 1587–1596.

[14]Brennenstuhl, U. and Hummel, D., "Vortex Formation over Double-Delta Wings," *International Council of the Aeronautical Sciences,* Paper 82-6.6.3, Aug. 1982.

[15]Fujii, K. and Schiff, L. B., "Numerical Simulation of Vortical Flows over a Strake-Delta Wing," *AIAA Journal,* Vol. 27, Sept. 1987, pp. 1153–1162.

[16]Turkel, E., "Improving the Accuracy of Central Difference Schemes," Institute for Computer Applications in Science and Engineering, ICASE Rept. 88-53, 1989.

[17]Matsushima, K., Takanashi, S., and Fujii, K., "Navier-Stokes Computations of Supersonic Flows about a Space-Plane," AIAA Paper 89-3502, Aug. 1989.